frontiers | Frontiers in Physics

TYPE Original Research
PUBLISHED 28 February 2024
DOI 10.3389/fphy.2024.1352134

OPEN ACCESS

EDITED BY
Lodovico Ratti,
University of Pavia, Italy

REVIEWED BY
Carlo Fiorini,
Polytechnic University of Milan, Italy
David Pennicard,
Helmholtz Association of German Research Centres (HZ), Germany
Dionisio Doering,
Stanford University, United States

*CORRESPONDENCE
Viktoria Hinger,
viktoria.hinger@psi.ch

RECEIVED 07 December 2023
ACCEPTED 07 February 2024
PUBLISHED 28 February 2024

CITATION
Hinger V, Barten R, Baruffaldi F, Bergamaschi A, Borghi G, Boscardin M, Brückner M, Carulla M, Centis Vignali M, Dinapoli R, Ebner S, Ficorella F, Fröjdh E, Greiffenberg D, Hammad Ali O, Hasanaj S, Heymes J, King T, Kozłowski P, Lopez-Cuenca C, Mezza D, Mozzanica A, Moustakas K, Paternoster G, Paton KA, Ronchin S, Ruder C, Schmitt B, Sieberer P, Thattil D, Xie X and Zhang J (2024), Resolving soft X-ray photons with a high-rate hybrid pixel detector.
Front. Phys. 12:1352134.
doi: 10.3389/fphy.2024.1352134

Resolving soft X-ray photons with a high-rate hybrid pixel detector

Viktoria Hinger[1]*, Rebecca Barten[1], Filippo Baruffaldi[1], Anna Bergamaschi[1], Giacomo Borghi[2], Maurizio Boscardin[2], Martin Brückner[1], Maria Carulla[1], Matteo Centis Vignali[2], Roberto Dinapoli[1], Simon Ebner[1], Francesco Ficorella[2], Erik Fröjdh[1], Dominic Greiffenberg[1], Omar Hammad Ali[2], Shqipe Hasanaj[1], Julian Heymes[1], Thomas King[1], Pawel Kozłowski[1], Carlos Lopez-Cuenca[1], Davide Mezza[1], Aldo Mozzanica[1], Konstantinos Moustakas[1], Giovanni Paternoster[2], Kirsty A. Paton[1], Sabina Ronchin[2], Christian Ruder[1], Bernd Schmitt[1], Patrick Sieberer[1], Dhanya Thattil[1], Xiangyu Xie[1] and Jiaguo Zhang[1]

[1]Paul Scherrer Institut, Villigen, Switzerland, [2]Fondazione Bruno Kessler, Trento, Italy

Due to their high frame rates and dynamic range, large area coverage, and high signal-to-noise ratio, hybrid silicon pixel detectors are an established standard for photon science applications at X-ray energies between 2 keV and 20 keV. These properties also make hybrid detectors interesting for experiments with soft X-rays between 200 eV and 2 keV. In this energy range, however, standard hybrid detectors are limited by the quantum efficiency of the sensor and the noise of the readout electronics. These limitations can be overcome by utilizing inverse Low-Gain Avalanche Diode (iLGAD) sensors with an optimized X-ray entrance window. We have developed and characterized a prototype soft X-ray iLGAD sensor bonded to the charge integrating 75 µm pixel JUNGFRAU chip. Cooled to −22°C, the system multiplication factor of the signal generated by an impinging photon is ≥ 11. With this gain, the effective equivalent noise charge of the system is ≤5.5 electrons root-mean-square at a 5 µs integration time. We show that by cooling the system below −50°C, single photon resolution at 200 eV becomes feasible with a signal-to-noise ratio better than 5.

KEYWORDS

hybrid detector, instrumentation for FEL, synchrotron radiation, LGAD, X-ray detector, low noise detector

1 Introduction

Photon science at soft X-ray energies (~200 eV–2 keV) at Synchrotron Radiation (SR) sources and Free-Electron Lasers (FELs) fosters a diverse spectrum of research. Experiments exploit the presence of the K and L-edges of light elements and 3d transition metals to study, for example, photosynthetic water splitting [1] and fundamental excitations that govern phenomena such as magnetic ordering [2] and high-temperature superconductivity [3] in correlated materials. For organic samples, experimental techniques that access the energy range between the carbon and oxygen K-edges, the so-called "water-window" (277–525 eV), are particularly relevant. However, while the technological capabilities of next-generation

X-ray sources are evolving at a rapid pace, detector systems are struggling to match the needs of experimental stations operating in the soft X-ray domain.

For many applications in the range of hard X-rays between ~2–20 keV, silicon hybrid detectors are the state-of-the-art. The high data quality and count rates of single photon counting systems such as PILATUS [4] and EIGER [5] allowed unprecedented advancements in terms of throughput and sensitivity for experiments at SR facilities. Charge integrating hybrid detectors that implement dynamic gain switching on the pixel level such as AGIPD [6], ePIX [7], and JUNGFRAU [8], on the other hand, provide the high sensitivity and dynamic range necessary for FEL-based diffraction, spectroscopy, and imaging experiments.

In the soft X-ray range, it has thus far been difficult to exploit hybrid detector technology. The reasons for this are twofold. First, because of the shallow absorption depth of low-energy X-ray photons, a significant percentage of photons are absorbed in the non-sensitive entrance window of the sensor, and the such generated charge does not contribute to the signal. Second, if a soft X-ray photon passes through the entrance window and generates a charge in the sensitive detector volume, the resulting signal is small compared to the electronic noise of the detector. As a result, a single photon cannot be discriminated from the noise floor.

Instead of standard hybrid detectors, scientists mainly use Charge Coupled Device (CCD) cameras [9–11] and CMOS image sensors [12–14] for soft X-ray detection. These systems can provide low noise (i.e., better than two electrons r.m.s. [15]) and high spatial resolution (down to 5 μm pixel size [16]) but are limited in terms of available detector area and frame rate capabilities. With the DSSC imager [17, 18], on the other hand, a system based on hybrid technology exists for the soft X-ray range. The detector is tailored to the high-rate bunch structure of EuXFEL but is limited in terms of spatial resolution. In light of the trend toward ultra-fast, high-throughput experiments at next-generation X-ray sources, the need for soft X-ray detector systems that match the sensitivity, spatial resolution, frame rate, dynamic range, and available detection area of hard X-ray hybrid detectors becomes especially apparent.

The recent development of inverse Low-Gain Avalanche Diode (iLGAD) sensors optimized for soft X-rays [19] opens the prospect for high-resolution hybrid detectors operating in this energy range. This approach addresses the two limitations of current hybrid technology. A thin entrance window maximizes the number of low-energy photons reaching the sensitive sensor volume, and the intrinsic gain of the iLGAD amplifies the signal of soft X-ray photons, allowing discrimination from the electronic noise floor of the hybrid detector.

In this work, we assess the capabilities of a soft X-ray hybrid detector based on the charge-integrating JUNGFRAU readout chip. Owing to their low noise and high dynamic range, JUNGFRAU systems are in operation at many facilities around the world, supporting a large variety of applications at FELs and high-flux SR experiments. Consequently, a soft X-ray version of the detector is of particular interest for applications at next-generation high-brilliance coherent light sources and high-rate FEL facilities. We present performance studies of a first JUNGFRAU-iLGAD prototype. The detector response to low-energy photons was investigated using X-ray fluorescence measurements with different metal targets. Taking these results as a baseline, we discuss the prospects of JUNGFRAU-iLGAD systems for soft X-ray applications.

2 Materials and methods

2.1 The JUNGFRAU detector

The hybrid silicon pixel detector JUNGFRAU [8] was primarily designed for the high-flux, pulsed conditions at FELs but has since extended its use also to SR sources [20, 21]. The readout chip provides a maximum frame rate of 2.2 kHz for continuous image readout and combines a charge-integrating architecture with three linear, dynamically switching gains per pixel. One chip comprises 256 × 256 pixels with a pixel size of 75 × 75 μm^2. A JUNGFRAU detector equipped with standard sensors and version 1.0 of the readout chip resolves single photons down to ~1.5 keV with an average noise level of 52 electrons (e^-) Equivalent Noise Charge (ENC) at a 5 μs integration time in low-noise high-gain mode (HG0). This corresponds to a Signal-to-Noise Ratio (SNR) of ~8 at 1.5 keV. The noise level stays well below the Poisson limit over the full dynamic range of 10^4 photons at 12 keV [8].

The most recent version of the readout chip, labelled JUNGFRAU 1.1, includes additional measures to reduce the noise to facilitate soft X-ray detection [22]. It achieves an average noise of 34 e^- r.m.s. in HG0 at a 5 μs integration time [22]–a 35% reduction compared to version 1.0.

2.2 Inverse Low Gain Avalanche Diodes (iLGADs)

LGAD sensors [23] were initially developed for applications in high energy particle tracking that require precision timing in the range of ~10 ps. The sensors include an additional implant of high doping concentration (~10^{16}–10^{17} cm^{-3}) below each sensor electrode. The resulting high electric field across the *p-n* junction promotes charge multiplication, amplifying the signal of an incoming particle or photon by a factor of 5–20 and generating an output signal proportional to the energy deposited in the sensor. This intrinsic signal amplification in the gain layer improves the SNR compared to a sensor without amplification.

However, standard LGADs for high energy physics cannot be used for photon science applications. This is due to two main reasons. To achieve better temporal resolution, the active sensors are usually thin (i.e., typically 50 μm) and therefore require a non-active carrier substrate on the back, which would block X-rays. Moreover, the fill factor of standard LGADs is less than 100% [24] because of the edge termination required to prevent premature voltage breakdown [25].

To make LGAD sensors suitable for soft X-ray detection, a number of design differences are required with respect to conventional LGADs for high energy physics. Inverse LGAD (iLGAD) sensors developed for soft X-rays [19] (Figure 1) are 275 μm thick and do not require any carrier substrate. They feature an optimized thin entrance window to improve the quantum efficiency at low photon energies. The entrance window

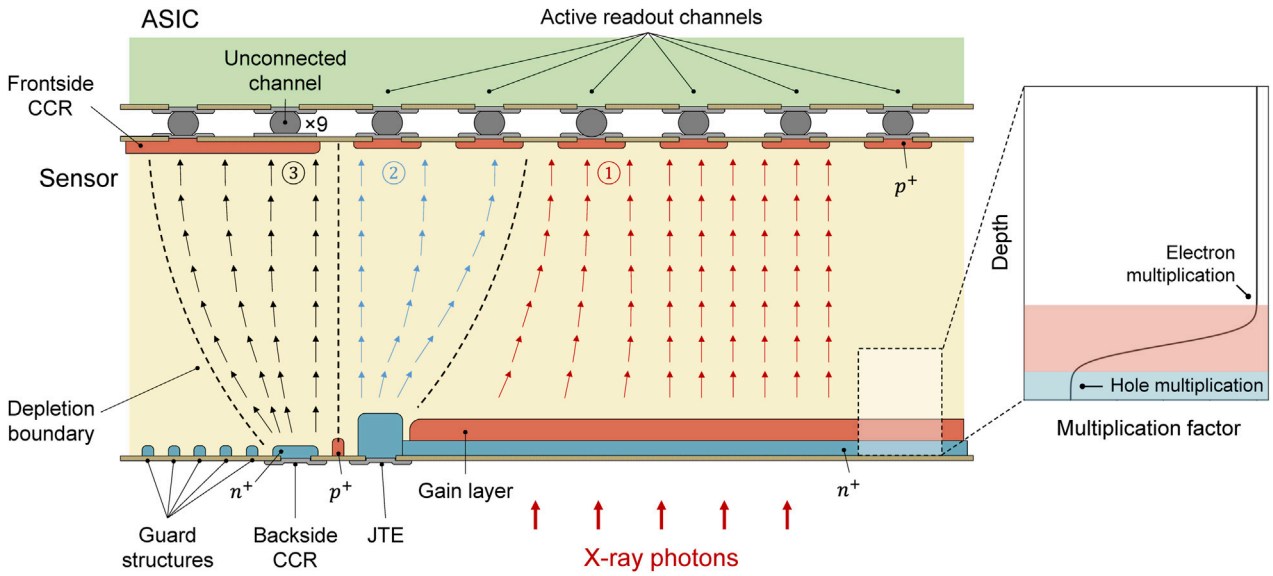

FIGURE 1
Schematic cross section of the edge of an iLGAD sensor and readout ASIC with indicated electric field lines. In the central region of the device (1), generated charge carriers travel through the gain layer and the pixels measure the amplified signal. In the border region (2), the generated charge carriers travel through the Junction Termination Extension (JTE) and, consequently, the pixels in this region measure the non-amplified signal. At the edge of the sensor, in region (3), the Current Collection Ring (CCR) or guard ring collects the generated charge carriers. The insert on the right shows the qualitative behaviour of the iLGAD multiplication factor as a function of the photon absorption depth, illustrating regions of hole-initiated and electron-initiated multiplication.

includes a surface passivation with thin SiO_2 and Si_3N_4 layers [26]. Moreover, the gain layer is continuous and located at the back of the sensor where X-ray photons enter (i.e., "inverse" to the conventional LGAD design, where the gain layer is segmented and located on the pixelated side of the sensor). In contrast to the conventional LGAD design, the inverse design provides a 100% fill factor and, with sufficiently small pixels, interpolation is possible, enabling a spatial resolution on the order of a micron [27]. This is required for several applications, including Resonant Inelastic X-ray Scattering (RIXS) experiments [28] at FELs and SR sources.

Because the gain layer of the iLGAD is located at the entrance window side, the multiplication factor depends on the photon absorption depth. This is illustrated in Figure 1. If a photon is absorbed before the gain layer, holes drift through the gain layer and initiate charge multiplication. In contrast, if the photon is absorbed beyond the gain layer, the multiplication is initiated by electrons. For photons absorbed within the gain layer, both electrons and holes initiate multiplication. The multiplication factors for electrons and holes differ depending on the gain layer design [29]. The first iLGAD R&D batch devised by the Paul Scherrer Institute (PSI) in collaboration with Fondazione Bruno Kessler (FBK, Trento, Italy) contains iLGADs with optimized thin entrance window and different gain layer designs labelled "standard," "shallow," and "ultra-shallow." For the "standard" gain layer design[1] investigated in this work, the hole multiplication factor is about 25% of the electron multiplication factor, as has been shown with simulations [19] and also reported in [29] with measurements. As a consequence of this design, hole multiplication is the dominant effect for photons with energies below about 500 eV.

2.2.1 JUNGFRAU-iLGAD prototype

For this work, we characterized the performance of a JUNGFRAU-iLGAD prototype. The iLGAD sensor was fabricated by FBK as part of the first iLGAD R&D batch targeting iLGADs for soft X-ray detection, devised in collaboration with PSI. The total size of the sensor is $2 \times 2\ cm^2$. It is made up of $75 \times 75\ \mu m^2$ pixels arranged in the standard 256×256 JUNGFRAU ASIC grid. On all sides of the grid, nine pixels are connected to the surrounding guard ring to collect the leakage current from the guard ring at the back and from the scribeline of the sensor (see Figure 1). This results in a total number of 238×238 active pixels. For the present study, a sensor with standard gain layer configuration was chosen because this design maximises the iLGAD multiplication factor. The sensor was bonded to a JUNGFRAU 1.1 readout chip (Figure 2). The quantum efficiency of the investigated iLGAD sensor and its gain layer design have been measured and reported by Liguori et al. [29].

2.3 Characterization measurements

The sensor-chip assembly was operated at a sensor bias voltage of 200 V and illuminated with fluorescence photons at a lab-based X-ray source. Four different secondary metal targets

1 The standard variation of the gain layer features a doping profile similar to that of LGADs used for high energy particle physics, which is not specifically optimized for soft X-ray detection.

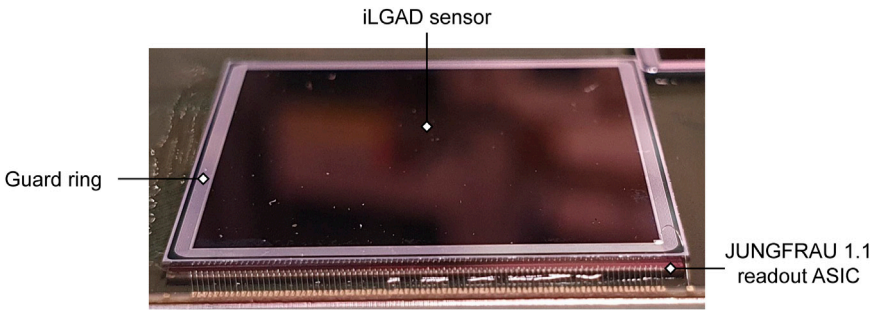

FIGURE 2
2 × 2 cm^2 iLGAD sensor bonded to a JUNGFRAU 1.1 readout chip.

were used to produce the fluorescence photons, namely, aluminium (K_α: 1.5 keV), titanium (K_α: 4.5 keV), chromium (K_α: 5.4 keV), and iron (K_α: 6.4 keV). These targets were chosen based on availability and considering the limitations of the lab-based setup to produce sufficient photon fluxes at lower energies. With this setup, the photon occupancy per single frame was at a level of 0.5%–4% for the investigated energies between 1.5 and 6.4 keV. The temperature of the system was regulated by means of a chiller connected to the front-end module with liquid coolant. The JUNGFRAU-iLGAD module was placed in a vacuum chamber flushed with nitrogen to a constant pressure of 10 mbar to prevent condensation at low temperatures and to minimize scattering and absorption of low-energy fluorescence photons before reaching the sensor.

Fluorescence spectra with a minimum of 10,000 images per acquisition point were taken for each metal target at eight chiller temperatures between −22°C and 15°C and at five different integration times between 5 µs and 100 µs. Datasets at a 10 µs integration time were acquired with higher statistics of > 200,000 images per temperature point. For each configuration, 1,000 dark images were acquired ahead of illumination with X-rays. The dark images are used to determine the signal offset (pedestal) and noise of each pixel. To account for the fact that the charge of a photon hit can be shared between neighboring pixels, the data were analysed using the cluster finding algorithm detailed in [30]. For all cases, the total charge generated by a photon hit is contained within a cluster of 2 × 2 pixels. Consequently, for the following analyses, we use the 2 × 2 clustered spectra.

3 Results

3.1 Gain

The signal response of each detector pixel to a photon hit of a given energy (i.e., the total gain g_{tot} of that particular pixel) is determined by two components: the conversion gain of the JUNGFRAU readout electronics g_{JF} and the multiplication factor M of the iLGAD. From these two components, g_{tot} is given as (Eq. 1)

$$g_{tot} = g_{JF} \times M. \quad (1)$$

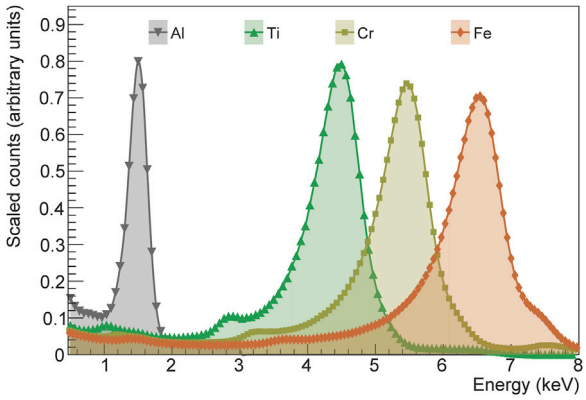

FIGURE 3
Energy calibrated fluorescence spectra (2 × 2 clusters) of four different metal targets (Al-K_α: 1.5 keV, Ti-K_α: 4.5 keV, Cr-K_α: 5.4 keV, Fe-K_α: 6.4 keV) acquired with the JUNGFRAU-iLGAD prototype at −22°C and 10 µs integration time. The energy calibration is performed on the pixel level with the Al-K_α peak as absolute reference point. The plot shows cumulative spectra across a region of 80 × 50 pixels.

We can determine the total gain of each pixel from a Gaussian fit to the measured spectra of the respective metal K_α-line as (Eq. 2)

$$g_{tot} = \frac{\mu_{K_\alpha}}{E_{K_\alpha}}. \quad (2)$$

Here, μ_{K_α} refers to the mean of the Gaussian in ADC units (ADU), and E_{K_α} is the nominal energy of the K_α-line. The pixel-wise calibrated fluorescence spectra obtained with the JUNGFRAU-iLGAD prototype are shown in Figure 3.

For the JUNGFRAU-iLGAD, we can separate the two components of the total gain by comparing the signal spectra of the pixels bordering the guard ring with the spectra of the central pixels. Because the gain layer terminates at the pixels next to the guard ring (see Figure 1), charge carriers generated in that region do not travel through the gain layer and the pixels detect the non-amplified signal.

Figure 4 illustrates the difference between the non-amplified spectrum of the border pixels and the amplified spectra of the central pixels at different temperatures. From the border pixel spectrum, we can calculate the conversion gain g_{JF} of the

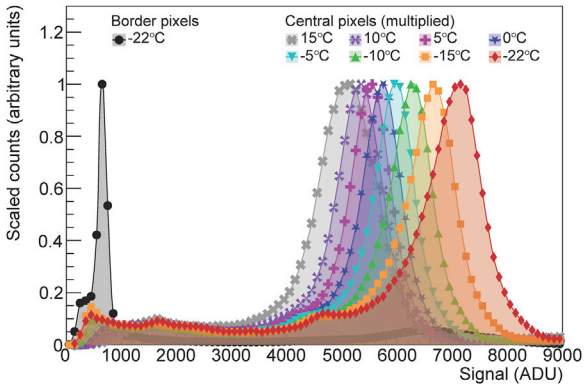

FIGURE 4
Clustered spectra of the Ti K_α-line (4.5 keV) in raw ADC units (ADU) measured with the JUNGFRAU-iLGAD prototype at a 10 µs integration time, with a noise cut-off at 5 × r.m.s. noise. Cumulative spectrum of the border region of the sensor (948 pixels) with the non-amplified signal at −22°C (black full circles) compared to the cumulative spectra across a region of 80 × 50 central pixels at varying temperatures, illustrating the temperature dependency of the multiplication factor.

JUNGFRAU readout electronics without iLGAD multiplication equivalent to Eq. 2 from a Gaussian fit to the signal peak. We chose the Fe-K_α peak as reference for the gain calculation because at this energy the separation of the signal peak from the noise is sufficiently high also for the non-amplified border pixel spectra at all temperatures. However, where gain calculation using the lower energy peaks as reference is possible, the obtained values agree within statistical uncertainties. Across all border pixels, the such calculated conversion gain is constant with an average value of $g_{JF} = 146.4 \pm 1.3$ ADU/keV for all investigated temperatures. The typical variations of the conversion gain across the full area of a JUNGFRAU module, found from measurements with standard silicon sensors, are in the range of 3.5% [31]. These pixel-to-pixel variations cannot be accounted for in the separation of conversion gain and iLGAD multiplication factor performed in this work.

To determine the iLGAD multiplication factor M, we compare the Fe-K_α peak positions of the border pixel spectrum and the signal spectra for each central pixel. From these measurements, M is given as (Eq. 3)

$$M = \frac{\mu_{\text{central}}}{\hat{\mu}_{\text{border}}}, \tag{3}$$

where μ_{central} is the per-pixel amplified peak position and $\hat{\mu}_{\text{border}}$ is the position of the non-amplified peak in the cumulative border pixel spectrum. The value of M varies across the area of the iLGAD (Figure 5A). In particular, we can identify two domains where the average values of M differ by about 10% (Figure 5B) with an approximate symmetry along one sensor diagonal. The dispersion of this distribution is much larger than the 3.5% variation of the JUNGFRAU conversion gain measured for standard sensors, and the magnitude of the difference between domains is too large to be congruent with temperature variations across the sensor. Consequently, we attribute the variations of M to variations in the doping composition of the gain layer.

The temperature trend of the multiplication factor is shown in Figure 6. We model the temperature dependency of M using a customized program that solves the one-dimensional Poisson equation, incorporating the doping profiles of the n^+ layer, the gain layer, and the doping concentration of the silicon bulk. Boundary conditions are set at 0 and 200 V, representing the bias voltages applied to the iLGAD sensor. This simulation determines the electric field distribution within the sensor, particularly in the charge multiplication layer. Subsequently, the multiplication factor M, initiated by electrons traveling through the gain layer, is calculated at various temperatures. The calculation utilizes the impact-ionization coefficient for electrons and holes, which are functions of the electric field distribution, employing the Okuto-Crowell model with the optimized

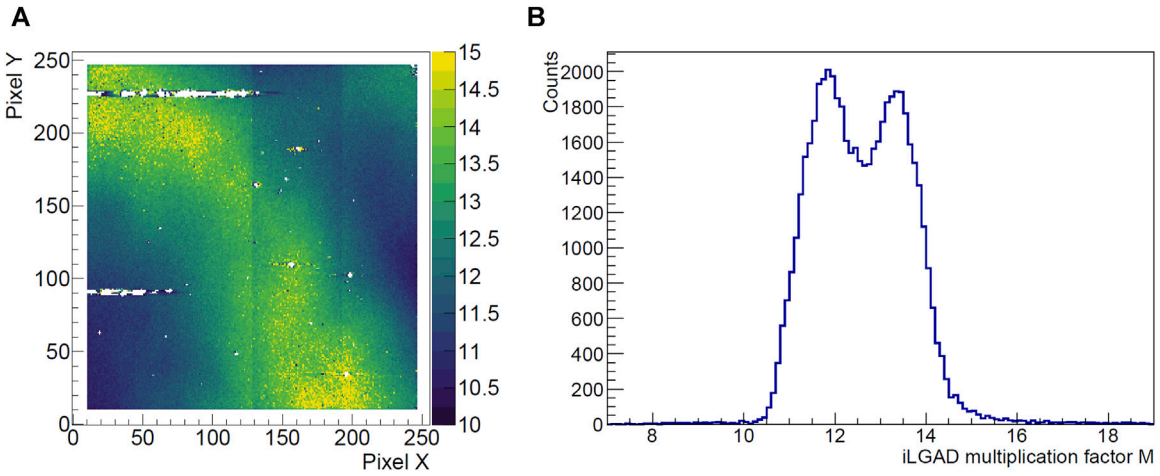

FIGURE 5
Variation of the iLGAD multiplication factor M across the 2 × 2 cm² sensor area measured at −22°C and a 10 µs integration time using the Fe-K_α line as absolute reference. **(A)** Pixel map of M. White regions indicate non-functional pixels (i.e., guard ring pixels, saturated, and dead pixels). The vertical artifacts are due to variations of the conversion gain of the chip. **(B)** Value distribution across all pixels, showing two different M domains.

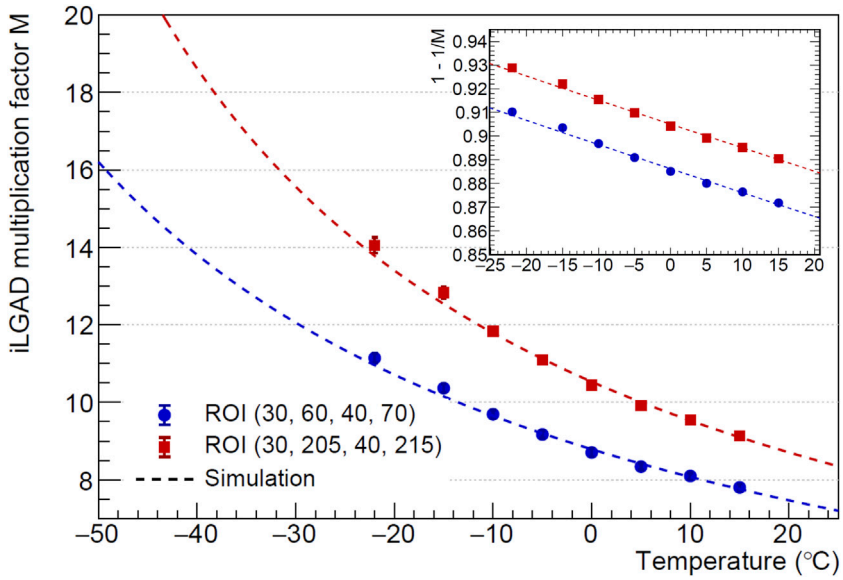

FIGURE 6
iLGAD multiplication factor M as a function of temperature. Comparison of measured values and simulation. The insert shows the linear behaviour of $1-\frac{1}{M}$. The measured data points correspond to the mean values of M within two 11 × 11 pixel ROI (x_{min}, y_{min}, x_{max}, y_{max}). Error bars represent the 1σ dispersion across all pixels of the ROI. For most data points, the dispersion is smaller than the plotted marker size.

parameters extracted by Currás Rivera and Moll [32]. The doping profile of the gain layer is obtained through Silvaco[2] process simulation, and its integrated dose is tuned until the simulated M aligns with the measurement results. The data points shown in Figure 6 correspond to the mean values of M within two different Regions Of Interest (ROI) of 11 × 11 pixels. We chose these small ROI to confine the modelling of M to regions with an approximately uniform distribution. In the simulation, we model the gain variations observed in the measurements by incorporating a difference of 1.25% integrated dose in the gain layer for the two ROI. The depth profile of the gain layer used in the simulation is the same for both ROI.

3.2 Leakage current

The leakage current of the iLGAD sensor represents an important contribution to the overall detector noise. Because of the presence of the gain layer, the leakage current is also multiplied. Moreover, in a charge integrating hybrid detector such as JUNGFRAU, in addition to the photon signal, the leakage current is integrated. Consequently, the SNR decreases with increasing integration time. Particularly for SR applications, which operate at long integration times to maximize the duty cycle of the detector, the leakage current becomes a performance limiting factor.

We determine the leakage current from dark images acquired at different temperatures and integration times. For each pixel, at each temperature, we fit a linear function to the average dark signal of 1,000 images as a function of integration time. The leakage current per pixel is then calculated from the slope of the fit for each individual pixel and the conversion gain of the JUNGFRAU electronics g_{JF} from Eq. 4:

$$I\,(\mathrm{A}) = \frac{\mathrm{slope}\ (\mathrm{ADU/ns})}{g_{JF}\ (\mathrm{ADU/keV})} \times \frac{1000\ (\mathrm{eV/keV})}{3.6\ \mathrm{eV}} \times q_0 \times 10^9\ (\mathrm{ns/s}). \quad (4)$$

Here, 3.6 eV is the average energy required to produce an electron-hole pair in silicon and q_0 is the elementary charge.

Figure 7 shows the temperature dependency of the leakage current for the same two ROI used in Section 3.1 and the average across the full sensor area. At 15°C, the average leakage current per pixel is 134 ± 18 pA and decreases to 5 ± 1 pA at −22°C. We note that the average leakage current across the full sensor area is higher than for both investigated ROI for most temperatures. This effect is due to the impact of hot pixels on the full-sensor average and is mitigated at lower temperatures. Plotted on a logarithmic scale, the leakage current displays a linear dependency on $1/T$. For a temperature difference of ~ 20°C, the leakage current changes by one order of magnitude. When lowering the operating temperature, the hybrid detectors using iLGAD sensors benefit from the lower leakage current and, consequently, lower noise and increased gain and, thus, a better SNR. Furthermore, we find that decreasing the operating temperature of the detector improves the pixel yield. For the investigated prototype, the average amount of non-functional pixels is 1.5% at 15°C decreasing to 0.8% at −22°C.

3.3 Effective detector noise

From the pedestal fluctuations σ for each pixel, we calculate the effective Equivalent Noise Charge (ENC_{eff}) in e^- as (Eq. 5)

2 https://silvaco.com/tcad

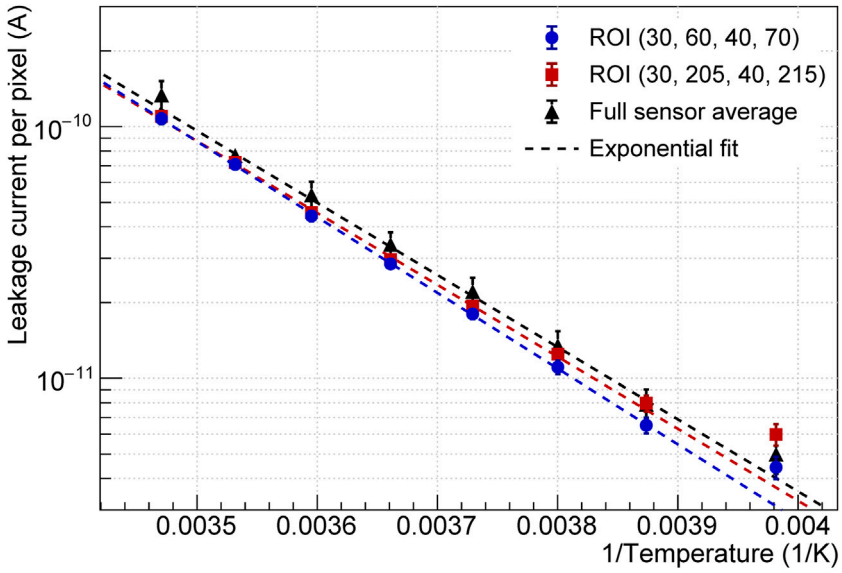

FIGURE 7
Leakage current of the JUNGFRAU-iLGAD as a function of the reciprocal of the temperature. Comparison of measured values and exponential fit. The measured data points correspond to the mean values within two 11 × 11 pixel ROI (x_{min}, y_{min}, x_{max}, y_{max}) and across the full sensor area. Error bars represent the 1σ dispersion across all pixels of the respective ROI.

$$\mathrm{ENC_{eff}}\ (e^-) = \frac{\sigma\ (\mathrm{ADU})}{g_{\mathrm{tot}}\ (\mathrm{ADU/keV})} \times \frac{1000\ (\mathrm{eV/keV})}{3.6\,\mathrm{eV}}. \qquad (5)$$

We show the average $\mathrm{ENC_{eff}}$ as a function of temperature for different integration times in Figure 8A and the corresponding average SNR for isolated 1 keV photons in Figure 8B. Both quantities follow an exponential trend as a function of temperature. At a 5 µs integration time and a temperature of −22°C, the JUNGFRAU-iLGAD system achieves an $\mathrm{ENC_{eff}}$ of 5.5 ± 0.7 e^- r.m.s., which corresponds to an SNR of 51 for single 1 keV photons when using single-pixel clusters. This becomes 25.5 for 2 × 2 clusters as the total noise of a cluster of N pixels scales with $\sqrt{N}$.

Figures 8C, D show the exponential trends extrapolated to lower temperatures. From this extrapolation, it can be estimated that in order to achieve an $\mathrm{ENC_{eff}}$ ~ 1 e^- r.m.s. at a 5 µs integration time, the system will need to be cooled to at least −60°C. At this low temperature, the influence of the shot noise diminishes because the leakage current is reduced strongly. As a consequence, the system noise at −60°C will be dominated by the ASIC noise, and the $\mathrm{ENC_{eff}}$ will be determined by the magnitude of the iLGAD gain. While the noise of the JUNGFRAU ASIC at such low temperatures needs to be verified experimentally, in a first, worst-case approximation, we can assume that it remains constant at the value of 34 e^- r.m.s. stated in [22]. Hence, with an iLGAD multiplication factor of M ~ 34, an $\mathrm{ENC_{eff}}$ ~ 1 e^- r.m.s. would be feasible. If the trend of M shown in Figure 6 is extrapolated to lower temperatures, a value $M > 30$ is realistic below ~ −60°C for the high-gain ROI. To verify this estimation, direct measurements of the noise of the JUNGFRAU-iLGAD system will need to be performed at lower temperatures.

Because of the dependency of the iLGAD multiplication factor on the photon absorption depth, the values stated above for the $\mathrm{ENC_{eff}}$ are only valid for photon energies for which electron-initiated multiplication dominates. For the standard gain layer design and normal photon incidence angle, electron multiplication dominates at energies >500 eV. At lower photon energies, hole multiplication becomes important and M reduces by about a factor four [29]. For 200 eV photons at −22°C, the SNR becomes 1.25 with clustering and 2.5 without. According to the extrapolation of the SNR for 1 keV photons shown in Figure 8D, we estimate that a SNR > 5 for 2 × 2 clustered data can be obtained at 200 eV with the investigated iLGAD sensor at a 5 µs integration time by cooling below ~ −50°C.

4 Discussion

The characterization results of the JUNGFRAU-iLGAD prototype demonstrate that this technology will enable hybrid detectors to advance into the soft X-ray domain. The present study constitutes the first characterization of a JUNGFRAU system employing iLGAD technology. It adds to previous investigations, which demonstrated the capabilities of the combination of an iLGAD sensor with the charge integrating, small pixel pitch MÖNCH chip [19]. With the sensor cooled to −22°C, this soft X-ray version of JUNGFRAU achieves an effective noise of 5.5 ± 0.7 e^- r.m.s. at a 5 µs integration time, which constitutes an improvement by a factor ~ 7 compared to the currently available best version of JUNGFRAU with standard silicon sensors. Achieving an SNR >5 for photon energies below 500 eV, for which hole-initiated multiplication dominates, will be possible by cooling the sensor to lower temperatures and exploiting the increase in multiplication factor with decreasing temperature.

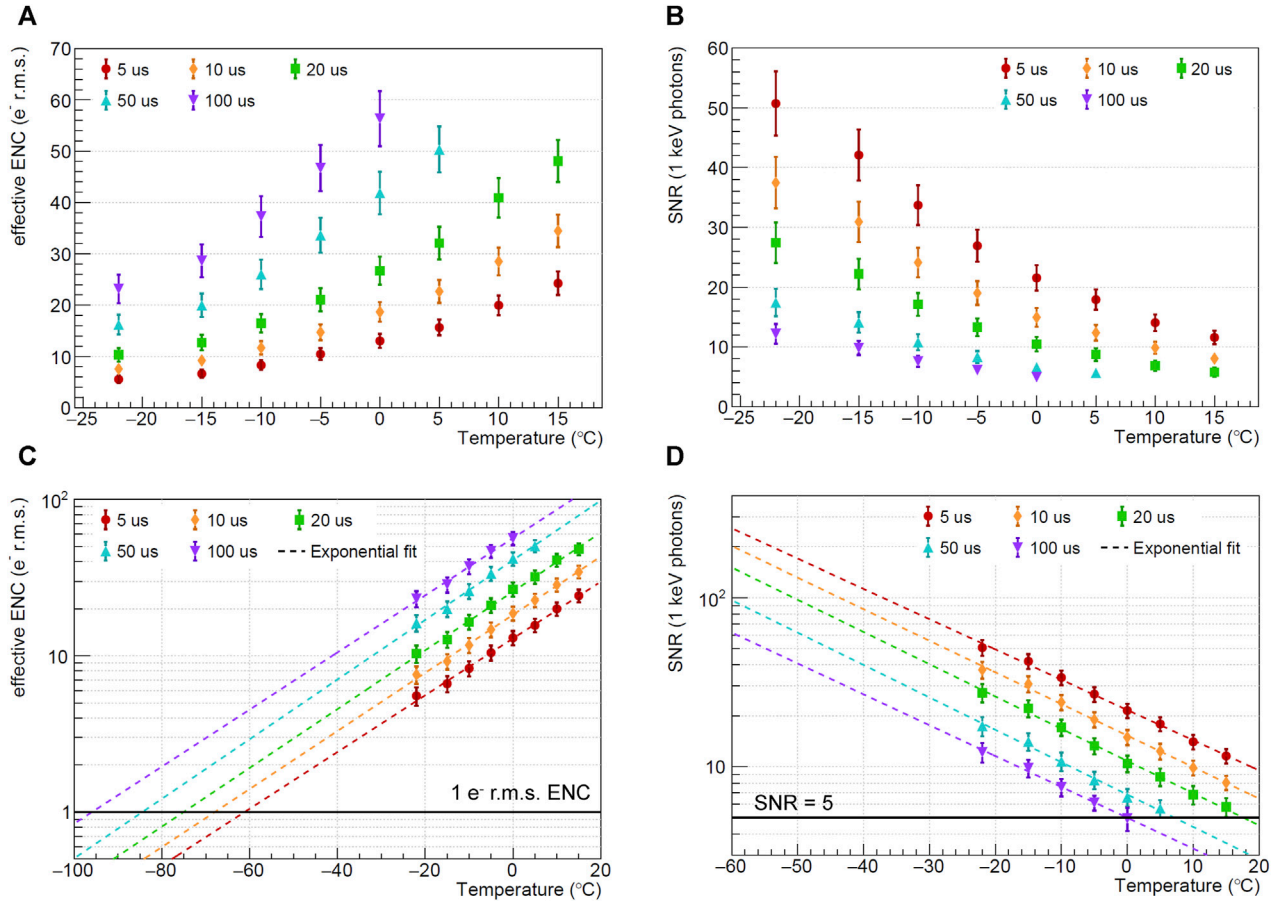

FIGURE 8
(A, C) Average effective ENC of the JUNGFRAU-iLGAD and **(B, D)** average SNR for 1 keV photons as a function of temperature for different integration times. Error bars represent the 1σ distribution across pixels. Panels **(C)** and **(D)** show the trends extrapolated to lower temperatures.

The present study also shows that iLGAD technology for soft X-ray applications can benefit from further optimization, particularly process improvements targeting a reduction of the leakage current, an increased uniformity of the gain layer, an increase of the pixel yield, and the improvement of the SNR at low photon energies (i.e., employing a shallow gain layer design to reduce the influence of hole-initiated multiplication). These optimizations will be addressed in future iLGAD R&D batches developed by the collaboration between PSI and FBK.

A JUNGFRAU-iLGAD system for soft X-rays opens possibilities for many photon science applications at FEL and SR sources alike. The 2.2 kHz frame rate of JUNGFRAU constitutes a more than thousandfold increase in speed compared to commercial CCD cameras for soft X-rays and at least a factor of 20 improvement compared to standard CMOS image sensors. The capability of JUNGFRAU 1.0 to acquire bursts of up to 16 images with an effective frame rate of ~ 150 kHz, opens further possibilities for high-rate applications with soft X-rays at next-generation FEL facilities [33]. Furthermore, with an area of 4 × 8 cm^2 for a 500 k pixel module, a JUNGFRAU system provides an active area that is eight times larger than standard CCD and CMOS devices. This can be further extended by tiling together multiple modules in customizable configurations. Especially for photon-starved spectroscopic techniques such as RIXS, a hybrid detector with high frame rate and large area would provide a significant improvement of the ratio between measurement time and acquired statistics. Additionally, the charge integrating architecture means charge sharing between neighboring pixels can be utilized to perform position interpolation, improving the spatial resolution of the detector beyond the pixel size. With the 25 µm pitch MÖNCH chip, for instance, spatial resolution in the micron range has been demonstrated in the hard X-ray domain [27, 34]. Based on these results, we note that an iLGAD hybrid detector based on the MÖNCH chip or an adapted version of JUNGFRAU with smaller pitch in one dimension would open further possibilities for spectroscopic techniques such as RIXS, soft X-ray spectro-ptychography, and soft or tender X-ray full field imaging techniques that rely on high spatial resolution.

Data availability statement

The raw data supporting the conclusion of this article will be made available by the authors, without undue reservation.

Author contributions

VH: Conceptualization, Data curation, Formal Analysis, Funding acquisition, Investigation, Methodology, Validation, Visualization, Writing–original draft, Writing–review and editing. RB: Resources, Writing–review and editing. FB: Formal Analysis, Validation, Visualization, Writing–review and editing. AB: Conceptualization, Data curation, Investigation, Project administration, Supervision, Validation, Writing–review and editing. GB: Resources, Writing–review and editing. MBo: Resources, Writing–review and editing. MBr: Resources, Writing–review and editing. MCa: Resources, Validation, Writing–review and editing. MCe: Resources, Writing–review and editing. RD: Resources, Validation, Writing–review and editing. SE: Resources, Writing–review and editing. FF: Resources, Writing–review and editing. EF: Resources, Software, Validation, Writing–review and editing. DG: Validation, Writing–review and editing. OH: Resources, Writing–review and editing. SH: Resources, Writing–review and editing. JH: Validation, Writing–review and editing. TK: Resources, Writing–review and editing. PK: Writing–Review and Editing, Resources. CL-C: Resources, Writing–review and editing. DM: Resources, Writing–review and editing. AM: Conceptualization, Data curation, Funding acquisition, Methodology, Resources, Supervision, Validation, Writing–review and editing. KM: Resources, Writing–review and editing. GP: Resources, Writing–review and editing. KP: Funding acquisition, Validation, Writing–review and editing. SR: Resources, Writing–review and editing. CR: Resources, Writing–review and editing. BS: Conceptualization, Funding acquisition, Project administration, Supervision, Validation, Writing–review and editing. PS: Resources, Writing–review and editing. DT: Resources, Writing–review and editing. XX: Validation, Writing–review and editing. JZ: Conceptualization, Formal Analysis, Methodology, Validation, Writing–review and editing.

Funding

The author(s) declare financial support was received for the research, authorship, and/or publication of this article. VH and KP received funding from MSCA PSI-FELLOW-III-3i (EU Grant Agreement No. 884104). Open access funding by PSI–Paul Scherrer Institute

Conflict of interest

The authors declare that the research was conducted in the absence of any commercial or financial relationships that could be construed as a potential conflict of interest.

The author(s) declared that they were an editorial board member of Frontiers, at the time of submission. This had no impact on the peer review process and the final decision.

Publisher's note

References

1. Ismail ASM, Uemura Y, Park SH, Kwon S, Kim M, Elnaggar H, et al. Direct observation of the electronic states of photoexcited hematite with ultrafast 2p3d X-ray absorption spectroscopy and resonant inelastic X-ray scattering. *Phys Chem Chem Phys* (2020) 22:2685–92. doi:10.1039/C9CP03374B

2. Elnaggar H, Wang RP, Lafuerza S, Paris E, Tseng Y, McNally D, et al. Magnetic contrast at spin-flip excitations: an advanced X-ray spectroscopy tool to study magnetic-ordering. *ACS Appl Mater Inter* (2019) 11:36213–20. doi:10.1021/acsami.9b10196

3. Barantani F, Tran MK, Madan I, Kapon I, Bachar N, Asmara TC, et al. Resonant inelastic X-ray scattering study of electron-exciton coupling in high-T_c cuprates. *Phys Rev X* (2022) 12:021068. doi:10.1103/PhysRevX.12.021068

4. Henrich B, Bergamaschi A, Broennimann C, Dinapoli R, Eikenberry E, Johnson I, et al. Pilatus: a single photon counting pixel detector for x-ray applications. *Nucl Instrum Meth A* (2009) 607:247–9. doi:10.1016/j.nima.2009.03.200

5. Tinti G, Bergamaschi A, Cartier S, Dinapoli R, Greiffenberg D, Johnson I, et al. Performance of the EIGER single photon counting detector. *J Instrumentation* (2015) 10:C03011. doi:10.1088/1748-0221/10/03/C03011

6. Kuster M, Boukhelef D, Donato M, Dambietz JS, Hauf S, Maia L, et al. Detectors and calibration concept for the European XFEL. *Synchrotron Radiat News* (2014) 27:35–8. doi:10.1080/08940886.2014.930809

7. Blaj G, Caragiulo P, Carini G, Carron S, Dragone A, Freytag D, et al. X-Ray detectors at the linac coherent light source. *J Synchrotron Radiat* (2015) 22:577–83. doi:10.1107/S1600577515005317

8. Mozzanica A, Bergamaschi A, Brueckner M, Cartier S, Dinapoli R, Greiffenberg D, et al. Characterization results of the JUNGFRAU full scale readout ASIC. *J Instrumentation* (2016) 11:C02047. doi:10.1088/1748-0221/11/02/C02047

9. Hall DJ, Soman M, Tutt J, Murray N, Holland A, Schmitt T, et al. Improving the resolution in soft X-ray emission spectrometers through photon-counting using an Electron Multiplying CCD. *J Instrumentation* (2012) 7:C01063. doi:10.1088/1748-0221/7/01/C01063

10. Kuster M, Ahmed K, Ballak KE, Danilevski C, Ekmedžić M, Fernandes B, et al. The 1-Megapixel pnCCD detector for the Small Quantum Systems Instrument at the European XFEL: system and operation aspects. *J Synchrotron Radiat* (2021) 28:576–87. doi:10.1107/S1600577520015659

11. Goldschmidt A, Grace C, Joseph J, Krieger A, Tindall C, Denes P. VeryFastCCD: a high frame rate soft X-ray detector. *Front Phys* (2023) 11. doi:10.3389/fphy.2023.1285350

12. Tamma C, Rota L, Caragiulo P, Markovic B, Segal J, Kwiatkowski M, et al. ePixM: a CMOS monolithic sensor for LCLS II. In: 2019 IEEE Nuclear Science Symposium and Medical Imaging Conference (NSS/MIC); 26 October 2019 - 02; Manchester, UK (2019). p. 1–4. doi:10.1109/NSS/MIC42101.2019.9059784

13. Marras A, Correa J, Lange S, Vardanyan V, Gerhardt T, Kuhn M, et al. Characterization of the Percival detector with soft X-rays. *J Synchrotron Radiat* (2021) 28:131–45. doi:10.1107/S1600577520013958

14. Léveillé C, Desjardins K, Popescu H, Vondungbo B, Hennes M, Delaunay R, et al. Single-shot experiments at the soft X-FEL FERMI using a back-side-illuminated scientific CMOS detector. *J Synchrotron Radiat* (2022) 29:103–10. doi:10.1107/S1600577521012303

15. Desjardins K, Medjoubi K, Sacchi M, Popescu H, Gaudemer R, Belkhou R, et al. Backside-illuminated scientific CMOS detector for soft X-ray resonant scattering and ptychography. *J Synchrotron Radiat* (2020) 27:1577–89. doi:10.1107/S160057752001262X

16. Andresen N, Bakalis C, Denes P, Goldschmidt A, Johnson I, Joseph JM, et al. A low noise CMOS camera system for 2D resonant inelastic soft X-ray scattering. *Front Phys* (2023) 11. doi:10.3389/fphy.2023.1285379

17. Porro M, Andricek L, Aschauer S, Castoldi A, Donato M, Engelke J, et al. The MiniSDD-based 1-mpixel camera of the DSSC Project for the European XFEL. *IEEE Trans Nucl Sci* (2021) 68:1334–50. doi:10.1109/TNS.2021.3076602

18. Castoldi A, Ghisetti M, Guazzoni C, Aschauer S, Strüder L, Hansen K, et al. Qualification of the X-ray spectral performance of the DEPFET pixels of the DSSC imager. *Nucl Instrum Meth A* (2023) 1057:168686. doi:10.1016/j.nima.2023.168686

19. Zhang J, Barten R, Baruffaldi F, Bergamaschi A, Borghi G, Boscardin M, et al. Development of LGAD sensors with a thin entrance window for soft X-ray detection. *J Instrumentation* (2022) 17:C11011. doi:10.1088/1748-0221/17/11/C11011

20. Leonarski F, Redford S, Mozzanica A, Lopez-Cuenca C, Panepucci E, Nass K, et al. Fast and accurate data collection for macromolecular crystallography using the JUNGFRAU detector. *Nat Methods* (2018) 15:799–804. doi:10.1038/s41592-018-0143-7

21. Leonarski F, Nan J, Matej Z, Bertrand Q, Furrer A, Gorgisyan I, et al. Kilohertz serial crystallography with the JUNGFRAU detector at a fourth-generation synchrotron source. *IUCrJ* (2023) 10:729–37. doi:10.1107/S2052252523008618

22. Hinger V, al Haddad A, Barten R, Bergamaschi A, Brückner M, Carulla M, et al. Advancing the JUNGFRAU detector toward low-energy X-ray applications. *J Instrumentation* (2022) 17:C09027. doi:10.1088/1748-0221/17/09/C09027

23. Pellegrini G, Fernández-Martínez P, Baselga M, Fleta C, Flores D, Greco V, et al. Technology developments and first measurements of Low Gain Avalanche Detectors (LGAD) for high energy physics applications. *Nucl Instrum Meth A* (2014) 765:12–6. doi:10.1016/j.nima.2014.06.008

24. Andrä M, Zhang J, Bergamaschi A, Barten R, Borca C, Borghi G, et al. Development of low-energy X-ray detectors using LGAD sensors. *J Synchrotron Radiat* (2019) 26:1226–37. doi:10.1107/S1600577519005393

25. Fernández-Martínez P, Flores D, Hidalgo S, Greco V, Merlos A, Pellegrini G, et al. Design and fabrication of an optimum peripheral region for low gain avalanche detectors. *Nucl Instrum Meth A* (2016) 821:93–100. doi:10.1016/j.nima.2016.03.049

26. Carulla M, Centis Vignali M, Barten R, Baruffaldi F, Bergamaschi A, Borghi G, et al. Study of the internal quantum efficiency of FBK sensors with optimized entrance windows. *J Instrumentation* (2023) 18:C01073. doi:10.1088/1748-0221/18/01/C01073

27. Cartier S, Kagias M, Bergamaschi A, Wang Z, Dinapoli R, Mozzanica A, et al. Micrometer-resolution imaging using MÖNCH: towards G_2-less grating interferometry. *J Synchrotron Radiat* (2016) 23:1462–73. doi:10.1107/S1600577516014788

28. Ament LJP, van Veenendaal M, Devereaux TP, Hill JP, van den Brink J. Resonant inelastic x-ray scattering studies of elementary excitations. *Rev Mod Phys* (2011) 83:705–67. doi:10.1103/RevModPhys.83.705

29. Liguori A, Barten R, Baruffaldi F, Bergamaschi A, Borghi G, Boscardin M, et al. Characterization of iLGADs using soft X-rays. *J Instrumentation* (2023) 18:P12006. doi:10.1088/1748-0221/18/12/P12006

30. Cartier S, Bergamaschi A, Dinapoli R, Greiffenberg D, Johnson I, Jungmann JH, et al. Micron resolution of MÖNCH and GOTTHARD, small pitch charge integrating detectors with single photon sensitivity. *J Instrumentation* (2014) 9:C05027. doi:10.1088/1748-0221/9/05/C05027

31. Redford S, Andrä M, Barten R, Bergamaschi A, Brückner M, Dinapoli R, et al. First full dynamic range calibration of the JUNGFRAU photon detector. *J Instrumentation* (2018) 13:C01027. doi:10.1088/1748-0221/13/01/C01027

32. Currás Rivera E, Moll M. Study of impact ionization coefficients in silicon with low gain avalanche diodes. *IEEE Trans Electron Devices* (2023) 70:2919–26. doi:10.1109/TED.2023.3267058

33. Sikorski M, Ramilli M, de Wijn R, Hinger V, Mozzanica A, Schmitt B, et al. First operation of the JUNGFRAU detector in 16-memory cell mode at European XFEL. *Front Phys* (2023) 11. doi:10.3389/fphy.2023.1303247

34. Chiriotti S, Barten R, Bergamaschi A, Brückner M, Carulla M, Chsherbakov I, et al. High-spatial resolution measurements with a GaAs:Cr sensor using the charge integrating MÖNCH detector with a pixel pitch of 25 μm. *J Instrumentation* (2022) 17:P04007. doi:10.1088/1748-0221/17/04/P04007